Along-axis hydrothermal flow at the axis of slow spreading Mid-Ocean Ridges: Insights from numerical models of the Lucky Strike vent field (MAR)

Fabrice J Fontaine, Mathilde Cannat, Javier Escartin, Wayne C. Crawford

AGU PUBLICATIONS

Geochemistry, Geophysics, Geosystems

RESEARCH ARTICLE
10.1002/2014GC005372

Key Points:
- The 3-D numerical models of MOR hydrothermal convection
- Detailed thermal regime of slow spread magma-rich segment center
- Relationships between flow geometry and earthquakes distribution

Supporting Information:
- Readme
- Appendix

Correspondence to:
F. J. Fontaine,
fontaine@ipgp.fr

Citation:
Fontaine, F. J., M. Cannat, J. Escartin, and W. C. Crawford (2014), Along-axis hydrothermal flow at the axis of slow spreading Mid-Ocean Ridges: Insights from numerical models of the Lucky Strike vent field (MAR), *Geochem. Geophys. Geosyst.*, *15*, 2918–2931, doi:10.1002/2014GC005372.

Received 8 APR 2014
Accepted 1 JUL 2014
Accepted article online 4 JUL 2014
Published online 22 JUL 2014

Along-axis hydrothermal flow at the axis of slow spreading Mid-Ocean Ridges: Insights from numerical models of the Lucky Strike vent field (MAR)

Fabrice J. Fontaine[1], Mathilde Cannat[1], Javier Escartin[1], and Wayne C. Crawford[1]

[1]Institut de Physique du Globe de Paris, CNRS, Paris, France

Abstract The processes and efficiency of hydrothermal heat extraction along the axis of mid-ocean ridges are controlled by lithospheric thermal and permeability structures. Hydrothermal circulation models based on the structure of fast and intermediate spreading ridges predict that hydrothermal cell organization and vent site distribution are primarily controlled by the thermodynamics of high-temperature mid-ocean ridge hydrothermal fluids. Using recent constraints on shallow structure at the slow spreading Lucky Strike segment along the Mid-Atlantic Ridge, we present a physical model of hydrothermal cooling that incorporates the specificities of a magma-rich slow spreading environment. Using three-dimensional numerical models, we show that, in contrast to the aforementioned models, the subsurface flow at Lucky Strike is primarily controlled by across-axis permeability variations. Models with across-axis permeability gradients produce along-axis oriented hydrothermal cells and an alternating pattern of heat extraction highs and lows that match the distribution of microseismic clusters recorded at the Lucky Strike axial volcano. The flow is also influenced by temperature gradients at the base of the permeable hydrothermal domain. Although our models are based on the structure and seismicity of the Lucky Strike segment, across-axis permeability gradients are also likely to occur at faster spreading ridges and these results may also have important implications for the cooling of young crust at fast and intermediate spreading centers.

1. Introduction

Geophysical constraints on the melt supply and near-axis lithospheric thickness along slow spreading ridges (spreading rate < 4 cm/yr) suggest that about 0.6 TW are available for on-axis hydrothermal heat extraction [see review in *Cannat et al*., 2004]. This heat is partly extracted through high-temperature ($>200°C$) hydrothermal vent fields, which have been found both at the center of magma-rich segments (e.g., Menez Gwen, Lucky Strike, Broken Spur, and Snake Pit vent fields) and at low-magma budget detachment faults within tectonically dominated segments (e.g., TAG, Rainbow, Ashadze, Logatchev). The present study focuses on magmatically dominated segment centers, particularly on the Lucky Strike vent field (37°18′N, 32°16′W) [*Langmuir et al*., 1997], where a seafloor observatory of tectonic, volcanic, hydrothermal, and biological processes has been in place since 2006 [*Cannat et al*., 2011]. The vent field is located on top of a large axial volcano (Figure 1) and is composed of approximately (i) 70 high-temperature (maximum $T = 330°C$), smoker-like vents and (ii) 1700 m^2 of associated diffuse flow venting. The total heat flux of the field is estimated to be between 200 and 1000 MW [*Barreyre et al*., 2012]. In addition, two more outflow areas have been identified, one ~2 km to the South and within the axial graben (the Evan site) [*M. Cannat, personal communication, 2014*], and another ~1.5 km to the East (the Capelinhos site) [*M. Cannat, personal communication, 2014*]. Both sites are limited in size and preliminary observations suggest that their heat output is negligible (less than a few MW) compared to the main Lucky Strike hydrothermal field.

Detailed geophysical and geological investigations stress the role of the local axial fault system on localizing high and low-temperature venting at Lucky Strike [*Ondréas et al*., 2009; *Barreyre et al*., 2012]. High-temperature vents and chimneys, low-temperature emanations and associated bacterial and faunal activities are mostly organized as clusters on the eastern and western parts of the faulted rim of a ~500 m wide paleo lava lake [*Fouquet et al*., 1995] bounded by a kilometer-wide axial graben [*Humphris et al*., 2002; *Ondréas et al*., 2009; *Barreyre et al*., 2012] (Figure 1). The heat is mined from a magma chamber located 3–4 km beneath the seafloor [*Singh et al*., 2006].

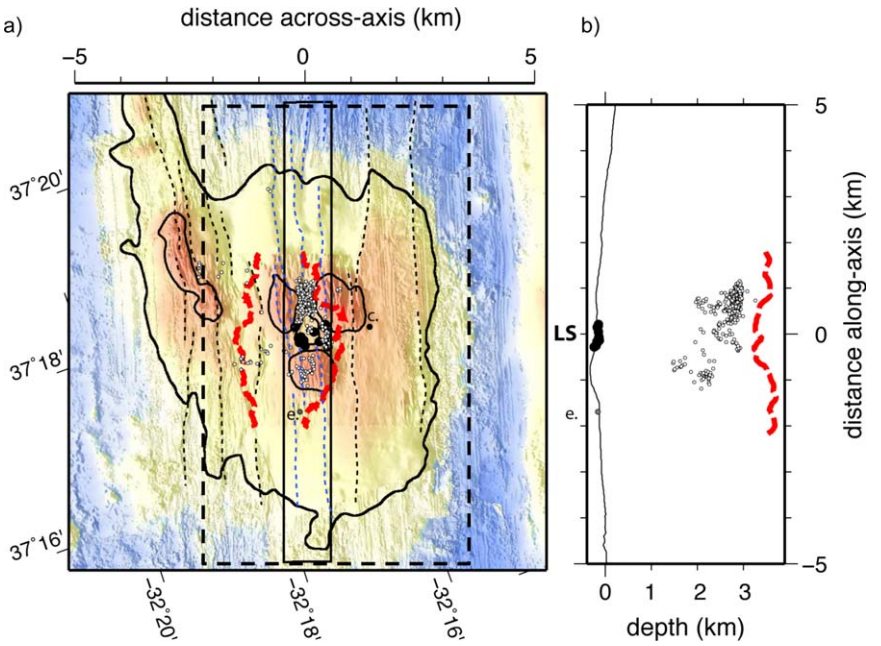

Figure 1. Lucky Strike volcano. Hydrothermal vent sites are indicated by black dots and relocated 2008–2009 hypocenters [*Crawford et al.*, 2013] by white dots. Red dashed lines mark the limits of the Axial Magma Chamber (AMC) reflector [*Singh et al.*, 2006]. (a) Map view. Solid contours are isodepths outlining the volcano base (−1900 m), the summit depression (−1710 m), and its three surrounding peaks (−1660 m). Red dashed lines mark the across-axis bounds of the AMC reflector and blue and black dashed lines mark significant surface faults (blue for the central highly fissured zone). Black boxes represent the bounds of the computational domain (dashed line) and the central fissure zone (solid line). The letters "c" and "e" stand for the Capelinhos and Evan hydrothermal sites. (b) Along-axis vertical section, with depths referred to 1.9 km beneath the sea surface. The black curve is the depth profile and the red dashed line the AMC reflector, both through the central lava lake and fissure zone (0 km across axis in Figure 1a). Hypocenters shown are located within the central fissured zone.

A microseismicity study provided constraints on the subseafloor hydrology. Using the 2007–2009 record of the Lucky Strike array of ocean bottom seismometers (OBS), *Crawford et al.* [2013] document microseismic clusters located just above the AMC, extending about a kilometer north and south of the main vent field and horizontally limited to beneath the main surface grabens extending from either side of the vent field. The small event magnitudes, clear depth limit and temporal continuity of these events over the 2 year experiment period lead the authors to interpret these clusters as due to cracking associated with thermal contraction at the base of two distinct hydrothermal recharge zones. A similar interpretation has previously been proposed for microearthquakes at the faster spreading Juan de Fuca ridge [*Sohn et al.*, 2004] and at the East Pacific Rise [*Tolstoy et al.*, 2008]. Microseismicity may thus be associated with cracking occurring in the brittle thermal boundary layer above the AMC (i.e., at temperatures $<$700–800°C) [*Hirth et al.*, 1998]. An alternative interpretation, also proposed for EPR microseismicity involves hydrothermal cooling causing crystallization and contraction of the AMC [*Sohn et al.*, 1999]. This alternative interpretation was not favored by *Crawford et al.* [2013] for the Lucky Strike microearthquakes clusters because the Lucky Strike events persisted for the full 2 years of seismic recording and because geodetic sensors installed over the same period did not detect any vertical ground motion [*Ballu et al.*, 2012]. In both interpretations, however, the observed clustering of microearthquakes, together with the position of the vent field, suggest an along-axis hydrothermal flow pattern at Lucky Strike, with privileged recharge areas located about a kilometer north and south of the active discharges [*Crawford et al.*, 2013].

This flow organization, with distinct upflow and downflow zones, departs from recent conceptual models of mid-ocean ridge high-temperature hydrothermal circulation inferred from numerical and mathematical analysis. *Coumou et al.* [2009a] describe a prototypical three-dimensional hydrothermal cell model in which vertical heat transport is optimized. In this model, the density contrast between low-viscosity hot ($T>$ ca. 300–350°C) and warm ($T<$ ca. 200–250°C) fluids drives circulation, so that colocated hot fluids rise and warm fluids sink in the crust. Conductive exchange between these fluids leads to the formation of a "nested-pipe geometry" composed of an outside warm recharge "duct" with temperature up to 200–250°C

immediately surrounding and feeding a hot, 350–400°C, upflowing pipe. *Coumou et al*. [2009a] argue that this flow organization prevails when small (<1 order of magnitude) permeability contrasts are imposed across axis in the models. This flow organization is thought to develop at one of the most extensively studied Mid-Ocean Ridge (MOR) vent fields, the Main Endeavour hydrothermal vent field at the intermediate spreading Juan de Fuca ridge, where magnetic and heat flux experiments [*Tivey and Johnson*, 2002] suggest that clusters of high heat flux smokers, which are regularly spaced every 200–300 m, are (i) fed by upflowing pipes that demagnetize the crust and (ii) immediately surrounded by heat flux lows due to recharge. The local flow organization suggested by *Coumou et al*. [2009a] does not, however, explain the along-axis hydrothermal cells proposed by *Crawford et al*. [2013]. In the present work, we use three-dimensional numerical models of hydrothermal convection to investigate the physical parameters that control the flow organization. We investigate the effect of thermal and permeability structures on hydrothermal flow dynamics, using scenarios constrained by geological and geophysical data from Lucky Strike volcano.

2. Model Geometry and Primary Results

2.1. Model Geometry

We introduce a series of numerical and physical models of hydrothermal activity based on the mathematical formalism described by *Rabinowicz et al*. [1998], in which three-dimensional numerical models of hydrothermal convection were developed, benchmarked, and then applied to calculate hydrothermal circulation and the associated heat flux distribution at Middle Valley, a sedimented segment along the Juan de Fuca ridge that hosts high-temperature, smoker-like activity. More recently, this formalism was applied to subaerial environments, including aerothermal flow (i.e., moist-air circulation) in the Piton de la Fournaise volcanic edifice (La Réunion Island) [*Antoine et al*., 2009].

Our three-dimensional modeling domain is designed to correspond to the dimensions of the Lucky Strike system, as shown in Figure 1. The model is 10 km long (L, *y* axis, along axis), 6 km wide (l, *x* axis, across axis), and 3 km deep (H, *z* axis). The hydrothermal flow model includes an open top boundary through which seawater is free to enter and leave. Top recharge temperatures are fixed at 2°C while discharge temperatures assume $\partial T/\partial z = 0$. The bottom boundary has a steady state temperature that can vary in space but is in every case $\leq$ 500°C. Side boundaries are impermeable and adiabatic ($\partial T/\partial y = \partial T/\partial x = 0$). Darcy's law controls fluid flow and the system's effective permeability, *k*, ranges between 10^{-15} and 4.5×10^{-14} m^2. This effective permeability represents a vertical average over the crustal section and leads to integrated vent field heat fluxes (i.e., the total heat flux vented at the top of the system) ranging from tens of MW to a few hundreds of MW, the latter values being commensurate with heat flux estimates of mid-ocean ridge high-temperature vent fields. The mathematical and numerical formalisms also allow for permeability variations in all directions. We use seawater-based temperature and pressure-dependent fluid properties as in several previous studies with two-dimensional geometries [e.g., *Fontaine and Wilcock*, 2007]. Although the models neglect phase separation of seawater and brine and vapor segregation at high temperatures (>~400°C), they provide a satisfactory description of the high-temperature, vapor-like, hydrothermal flows typical of Lucky Strike (most high-temperature venting fluids at Lucky Strike have salinities lower than that of seawater [e.g., *Charlou et al*., 2000; *Pester et al*., 2012]) as stated by *Geiger et al*. [2005] and *Fontaine and Wilcock* [2007] (see also section 5). Details about the numerical procedure to solve the convection equations are given in *Rabinowicz et al*. [1998] and summarized in Appendix 1 of supporting information (see also Table 2 for a list of model parameters and symbols). In the following sections, we calculate fluid circulation for a homogeneous model and test the effect of variations in across and along-axis permeability and basal temperature on the geometry of hydrothermal flow.

2.2. Three-Dimensional Uniform Permeability Models

Figure 2 shows the results of a numerical experiment in which we impose a uniform permeability ($k = 0.75 \times 10^{-14}$ m^2) throughout the modeling domain and a constant bottom temperature ($T_{bot} = 500$°C). Integrated vent heat flux is 350 MW (Table 1). This heat is discharged at about fifteen 1 km wide venting sites (Figure 2a), overlying pipe-like hydrothermal upflow zones (Figure 2b). Maximum venting temperatures are about 380°C (Figure 2a) at the center of individual pipes. This first experiment highlights a basic dynamical feature of three-dimensional high-temperature hydrothermal circulation within young oceanic crust [*Coumou et al*., 2009a]: the occurrence of warm recharge zones (~200°C) coating hot (~380°C) upflowing pipes (Figure 2a). This pattern is due to the nonlinear thermodynamic properties of (sea)water (see section 1).

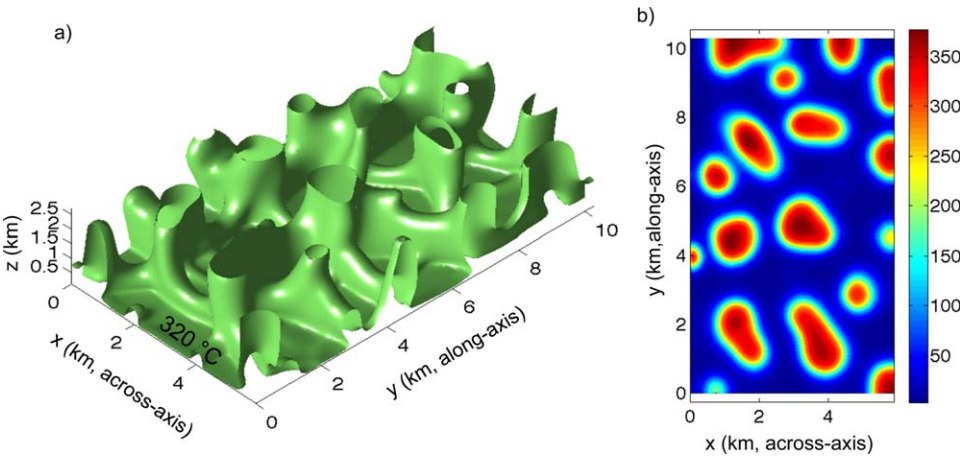

Figure 2. Model results for a simulation with a permeability field ($k = 0.75 \times 10^{-14}$ m^2) and constant bottom temperature ($T_{bot} = 500°C$). (a) The 320°C isotherm in the model box. The *z* axis represents distance above model bottom. (b) Top surface temperature field.

However, the random distribution of venting areas in Figure 2 does not fit with the actual distribution of vents at Lucky Strike or with the along-axis oriented hydrothermal cells inferred from the microseismicity data [*Crawford et al*., 2013].

3. Influence of Across-Axis Basal Thermal Gradients

Numerical models by *Coumou et al*. [2009a] have shown that hydrothermal sites will be distributed roughly along-axis, with recharge in between vent areas, if the hydrothermal layer is not uniformly heated from the bottom but is instead supplied with a significantly higher heat flux in a < 1 km wide axial region. This configuration generates across-axis temperature gradients at the base of the hydrothermal layer, which influence the rise of convective thermal instabilities. This model geometry likely mimics the limited across-axis extent of the axial magma chamber at fast/intermediate spreading axes. To account for the larger (3–4 km wide) across-axis extent of the Lucky Strike axial magma chamber [*Singh et al*., 2006; *Crawford et al*., 2010] (Figure 1), we test the effects of various across-axis horizontal temperature gradients at the base of our hydrothermal layer (Figure 3).

Table 1. Summary of Numerical Simulations[a]

Description	Permeability (m^2)	$\Delta T_{across\text{-}axis}$ (°C/km)	d_{slot} (km)	I (MW)
Constant Basal T and Permeability				
(Figure 2)	0.75×10^{-14}			350
Across-Axis Basal T Gradient Models				
	1.5×10^{-14}	~65		396
(Figure 5)	3.0×10^{-14}	~65		720
	4.5×10^{-14}	~65		780
	1.5×10^{-14}	~130		302
(Figure 4)	3.0×10^{-14}	~130		480
	4.5×10^{-14}	~130		590
Heaviside-shape	1.5×10^{-14}			490
Across-Axis Permeability Gradient Models				
	$[0.07–1.5] \times 10^{-14(*)}$		3	81
	$[0.15–1.5] \times 10^{-14(*)}$		3	110
Across-Axis Basal T and Permeability Gradient Models				
(Figure 6)	$[0.225–4.5] \times 10^{-14(*)}$	~65	3	217
	$[0.15–3] \times 10^{-14(*)}$	~65	3	156
	$[1.5–3] \times 10^{-14(*)}$	~65	3	450
	$[0.3–3] \times 10^{-14(*)}$	~65	3	190
	$[0.6–3] \times 10^{-14(*)}$	~65	3	240
	$[0.1–1.5] \times 10^{-14(*)}$	~65	0.9	52

[a]I: Integrated vent heat flux (MW), $\Delta T_{across\text{-}axis}$: Across-axis basal temperature gradients, d_{slot}: depth extent of the axial high-permeability slot, and (*): the higher value is in the axial slot, the lower value in the hosting crust.

Figures 4 and 5 show the results of numerical experiments performed with the "Gaussian-like" configurations of Figure 3. This approach is similar to the one presented in *Coumou et al*. [2009a]. Across axis, the maximum basal temperature ($T_{bot} = 500°C$) is located at the center of the modeling domain, and we investigate the effects of the basal temperature profile width (Figure 3). Besides these Gaussian-like profiles, we also discuss results from models with a "Heaviside-like" shape (Figure 3), which could be more appropriate in contexts with wide and subhorizontal AMC roofs, like Lucky Strike.

Figure 4 shows the results of a simulation using the narrower Gaussian-like basal temperature anomaly (dashed line, Figure 3). This model, whose maximum basal temperature gradient is

Table 2. List of Symbols

Parameter	Name	Units	Value
Roman			
T	Temperature	°C	[0–500]
P	Pressure	Pa	[200–500] $\times 10^5$
L (x)	Model width	m	6×10^3
l (y)	Model length	m	10^4
H (z)	Model depth	m	3×10^3
g	Gravity	m s^{-2}	9.8
K	Permeability	m^2	[0.1–4.5] $\times 10^{-14}$
K_0	Reference permeability	m^2	10^{-14} m^2
U	Horizontal velocity (x)	m s^{-1}	
V	Horizontal velocity (y)	m s^{-1}	
W	Vertical velocity (z)	m s^{-1}	
t	Time	s	
c_m	Matrix heat capacity	J kg^{-1} °C^{-1}	
c_f	Fluid heat capacity	J kg^{-1} °C^{-1}	
R	Hydraulic resistivity	m s^{-1}	
R_0	Reference hydraulic resistivity	m s^{-1}	
Ra	Rayleigh number		[100–400]
Greek			
μ	Fluid viscosity	Pa s	
μ_0	Fluid reference viscosity	Pa s	1.8×10^{-3}
λ	Matrix conductivity	W °C^{-1} m^{-1}	1.5
γ	Heat capacity ratio		0.75
κ	Matrix diffusivity	m^2 s^{-1}	6×10^{-7}
ρ_f	Fluid density	Kg m^{-3}	
ρ_m	Matrix density	Kg m^{-3}	
ρ_0	Fluid reference density	Kg m^{-3}	1036

approximately 130°C/km, generates a venting heat flux of 480 MW (Table 1) that is extracted by a kilometer-wide (across-axis), "sheet-like," vertical upflow zone extending along the entire model length. The maximum venting temperature of about 300°C is located at the center of the sheet-like upflow zone (Figure 4a). Recharge occurs across axis with warm (150–200°C), continuous (along-axis), sheet-like downflow zones that coat the central upflow on both sides (Figure 4b).

Figure 5 shows the results of a simulation using a wider Gaussian-like basal temperature anomaly (solid line, Figure 3). This model has one-half the maximum basal temperature gradient of the previous model: approximately 65°C/km. The planar circulation of Figure 4 destabilizes into a pipe-like circulation (Figure 5c) and the venting heat flux increases to about 720 MW (Table 1), 50% higher than for the narrower basal temperature anomaly. The heat is extracted through a series of discrete venting sites along the axis, some of them (e.g., V1 = 195 MW in Figure 5a) with a pipe-like root, whereas others integrate two or more coalescing upwelling zones/pipes and have an irregular shape that is elongated along-axis (e.g., V2 = 316 MW and V3 = 216 MW in Figure 5a). Preferential recharge occurs in warm (200°C) downflows that coat each hot (350°C) venting zone/pipe (Figure 5b). Simulations run with the "Heaviside-like" basal temperature profile (not shown in this section but discussed in section 5) produce a similar "nested-pipe" flow organization with along-axis orientation and, for a model permeability of 1.5×10^{-14} m^2, the venting heat flux is 490 MW (Table 1). These simulations highlight the central role of basal horizontal thermal gradients on producing discrete, along-axis oriented, venting sites. The flow organization in our models agrees with the simulations of *Coumou et al.* [2009a] and we concur with them that, if basal heat flux increases (i.e., permeability increases throughout the model), the pipe-like pattern will become prominent as the elongated venting sites observed in our simulation progressively split into discrete pipe-like structures surrounded by warm downflows (like V1).

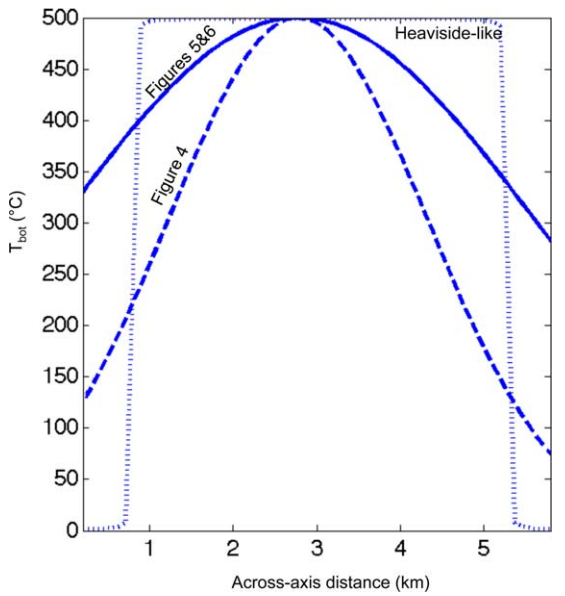

Figure 3. Across-axis bottom temperature profiles for subsequent simulations in this study.

4. Influence of the Permeability and Basal Temperature Structures

Along-axis flow organization resulting from across-axis permeability contrasts was first postulated based on seismic tomography results for the CoAxial

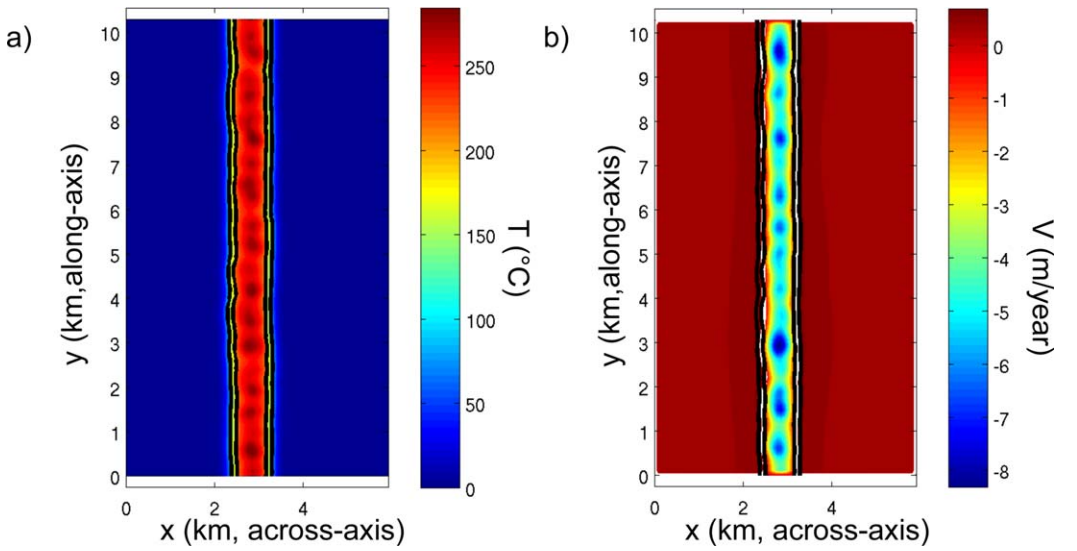

Figure 4. Model results for a simulation with spatially homogeneous permeability ($k = 3 \times 10^{-14}$ m^2) and a narrow, "Gaussian-like," across-axis bottom temperature gradient (dashed profile in Figure 3). (a) Top surface temperature field. Black lines mark the 100°C and 200°C isotherms. (b) Top surface Darcian velocity field. Negative and positive values refer to upflow and downflow velocities, respectively. White lines (mostly in between the black 100°C and 200°C isotherms) represent the transition between upflow and downflow.

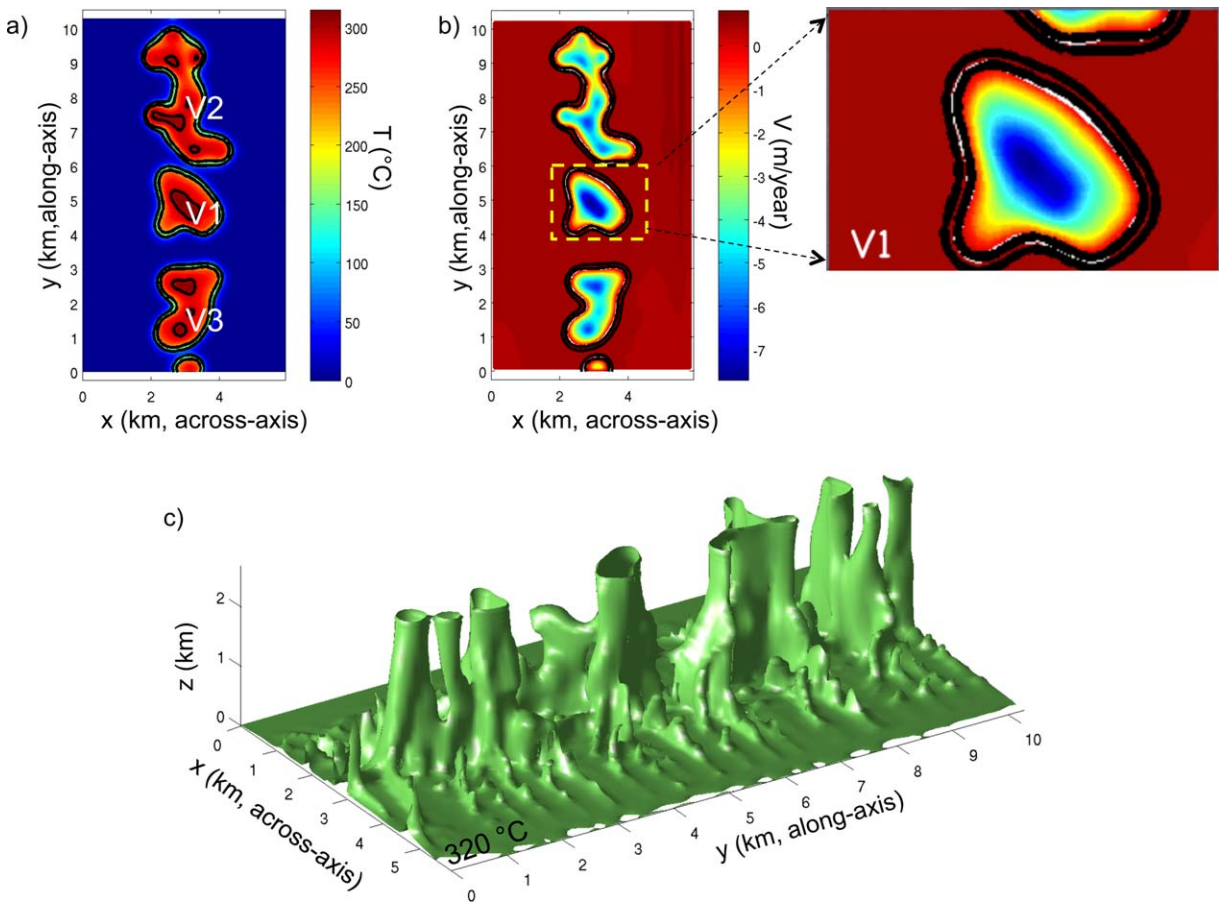

Figure 5. Same as Figure 4 but for a wider across-axis bottom temperature profile (solid line, Figure 3). (a) Top surface temperature field. (b) Same as Figure 4b, plus a zoom on the top surface structure of the V1 pipe. Note that the upflow/downflow transition (white line) occurs locally at $T > 200$°C. (c) The 320°C isotherm in the model box.

segment of the Juan de Fuca Ridge [*Sohn et al*., 1997]. Detailed geological studies indicate that the preferred location of hydrothermal venting along mid-ocean ridges is the highly deformed axial zone where the crust is densely fractured, faulted, and fissured and therefore likely to be much more permeable [e.g., *Hearn et al*., 2013]. Numerical models by *Coumou et al*. [2009a] show, however, that a small (<1 order of magnitude) across-axis linear decrease in permeability does not influence the "nested-pipe" flow organization. *Rabinowicz et al*. [1999] also inferred pipe-like discharge zones ("fingers") for a very different model based on fast spreading ridges: a permeable along-axis slot that is no more than 100 m wide and is bounded by impermeable walls. The finger-like flow geometry in this model is controlled by the narrow width of the fractured slot [*Rabinowicz et al*., 1999] and the pressure/temperature-dependent fluid viscosity and expansivity [*Rabinowicz et al*., 1998]. This slot geometry does, however, force a two-dimensional, along-axis, circulation pattern.

We test here the effects of an along-axis permeable zone that (i) is wider and smoother than that modeled by *Rabinowicz et al*. [1999] and (ii) can have a permeability contrast larger than those considered by *Coumou et al*. [2009a]. The Lucky Strike venting area is crosscut by a dense network of normal faults [e.g., *Scheirer et al*., 2000; *Escartin et al*., 2006; *Ondréas et al*., 2009], concentrated in a km-wide axial graben along the axial valley that dissects the main volcanic edifice (Figure 1). To mimic this central fissure network and study its first-order effects on flow dynamics, we introduce a kilometer-wide high-permeability slot in the center of our model, reaching from the seafloor to the base of the model. We discuss the validity of this vertical continuity later in the section 5. Because there are no direct constraints on the permeability contrast between the «fissure-zone» and the adjacent rock, this contrast is a free parameter in our experiments.

Figure 6 shows the results of experiments in which the central fissure zone has a permeability of 4.5×10^{-14} m^2 and the permeability contrast is 20. Basal heating is the same as in the model of Figure 5 (65°C/km across axis). For this experiment, the venting heat flux is 217 MW (Table 1), extracted through three discrete (V1 = 70 MW, V2 = 60 MW, V3 = 87 MW), kilometer-wide venting sites corresponding to upflowing vertical pipes (Figures 6a and 6c). Interestingly, the maximum recharge velocities are not in the warm (150–200°C) areas immediately around the upflowing pipes, as was the case in the constant permeability simulations [*Coumou et al*., 2009a] (Figures 4b and 5b), but are instead distributed along-axis between outflow zones (Figure 6b). This change is a result of the lowered efficiency of off-axis recharge, requiring enhanced along-axis recharge in order to conserve mass.

This permeability structure also impacts heat and mass flux distributions at the top of the modeling domain (Figure 7). In constant permeability models (Figures 7a and 7b), zones of maximum recharge mass flux (Figure 7a) and heat flux (Figure 7b) are both located in the warm halo immediately coating the discharging pipes. In contrast, in models with a central high-permeability slot (Figures 7c and 7d), these zones are separated. The maximum recharge heat flux is still around the upflowing pipes (Figure 7d) but the recharge mass is distributed along axis (Figure 7c). The highly permeable axial zone enhances the inflow of cold and dense seawater away from the discharging pipes.

We evaluated the effect of varying different parameters of the model on the generation of this along-axis recharge and pipe-like upwelling behavior. The basal heating profile has a strong effect on the permeability contrast that is needed between the slot and the surrounding rock in order to generate this behavior: a contrast of at least 10 is needed if basal heating is uniform, whereas a contrast of 2 is sufficient for the narrow Gaussian-like basal temperature distribution of Figures 3 and 4. If we limit the vertical extent of the central permeable zone to the top 0.9 km of the model (not shown in the figures, but listed in Table 1) the venting areas become smaller, because the upflowing pipes narrow when entering this higher-permeability superficial fissure network, in agreement with two-dimensional models [e.g., *Wilcock*, 1998]. Also in our models, and consistent with analytical arguments [e.g., *Lowell and Germanovich*, 2004], the extracted heat flux increases when the width and/or the permeability of the axial fissured zone increases, or when the permeability outside the fissured zone increases (Table 1).

Figure 8 shows the heat extraction (in W/m^2) at the base of the hydrothermal layer for models with and without a low-permeability slot and with either a Gaussian or Heaviside basal temperature gradient. Figure 8a corresponds to the model presented in Figures 5 and 8c corresponds to the model presented in Figure 6. The models with constant permeability (Figures 8a and 8b) have complex spatial heat extraction patterns because of the 3-D recharge network around the discharging pipes (as in Figure 5). The models with both

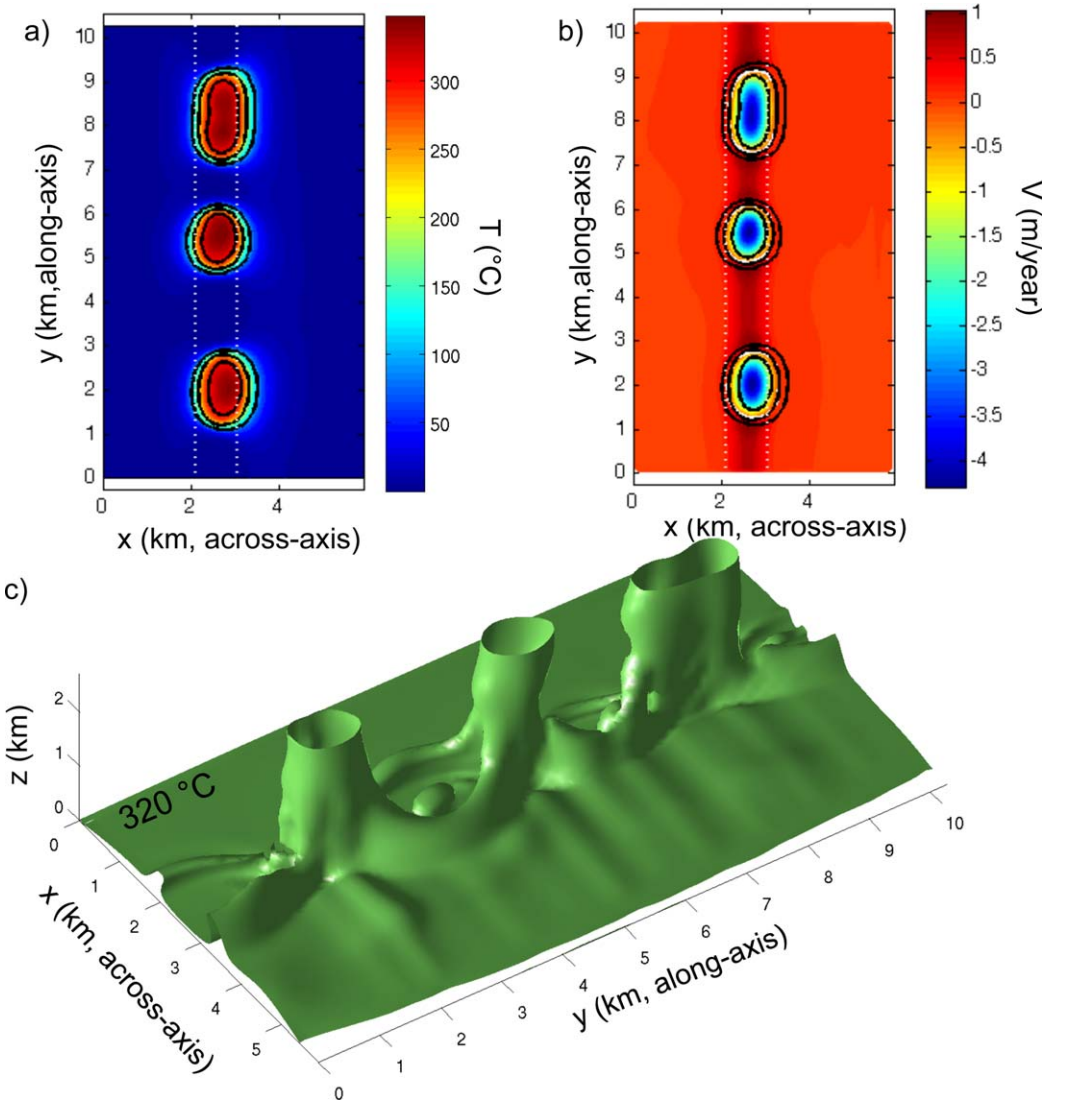

Figure 6. Model results for a simulation with the same across-axis bottom temperature gradients as in Figure 5, plus a central slot whose permeability is 4.5×10^{-14} m^2 (20 times higher than outside the slot). Dashed white lines represent the trace of the slot at the top of the model. (a) Top surface temperature field. V1, V2, and V3 refer to vent fields. (b) Top surface Darcian velocity field. (c) The 320°C isotherm in the model box.

basal temperature and across-axis permeability gradients (Figures 8c and 8d), on the other hand, display a well-organized heat extraction pattern, with along-axis oriented, km-wide alternating zones of heat flux highs and lows matching the base of recharge and discharge areas, respectively. Models with across-axis permeability gradients but constant basal temperature (not shown) display the same well-organized heat extraction pattern if the permeability contrast is greater than 10.

5. Discussion

The primary reason why the base of recharge and discharge zones in Figures 8c and 8d are heat flux highs and lows, respectively, is that the bottom thermal boundary layer—where cold fluids are heated up along the convective path—is thinner below recharge zones than below discharge zones. Heat flux extraction amplitudes vary by more than 1 order of magnitude between highs/recharges and lows/discharges when the permeability ratio between the fractured slot and the surrounding rocks exceeds 10 (Figure 8), consistent with the predictions of two-dimensional numerical models by *Fontaine et al*. [2011]. We propose that the circulation pattern produced by across-axis permeability (and possibly basal temperature) gradients

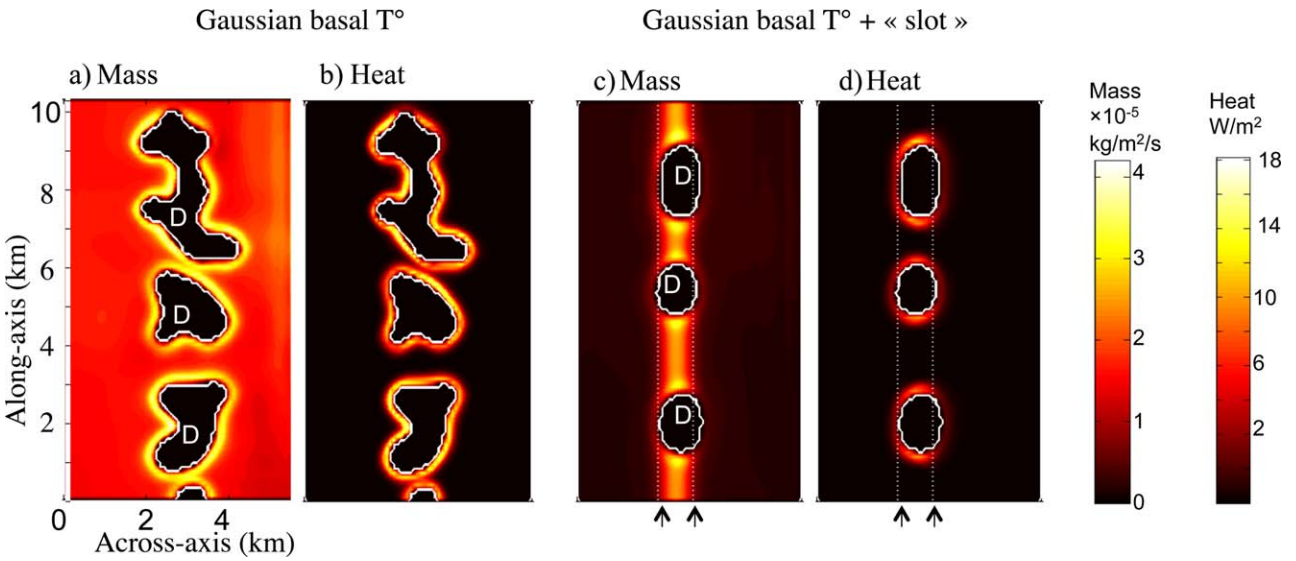

Figure 7. Recharge mass and heat flux at the top surface of models presented in Figures 5 and 6. White lines refer to the upflow/downflow transition. D: Discharge. (a and b) Model with bottom temperature gradients only: zones of maximum recharge mass flux coincide with zones of maximum recharge heat flux in the yellow halo around the pipe-like structure. (c and d) Same model, plus a higher-permeability slot: maximum heat fluxes still coincide with the pipes, but mass recharge is more widely distributed along axis. Black arrows and the dashed white lines show the limits of the higher-permeability slot.

explains the seismicity hypocenter distribution at Lucky Strike, where earthquake clusters are observed approximately 1 km North and South of the main active field [*Crawford et al*., 2013]. We propose that heat extraction highs below recharge zones have enhanced microearthquake activity, whereas heat extraction lows below discharge zones have little or no microearthquake activity. We also infer that the hydrothermal flow geometry in the Lucky Strike crust is controlled to a large extent by across-axis permeability variations.

Crawford et al. [2013] also noted clusters of seismicity beneath and to the sides of the hydrothermal field, which were active only during a 3 month "swarm" of increased earthquake activity. These clusters may have been activated by an increase in hydrothermal flow associated with this swarm, which would increase the basal heat flux and generate cooling-related lithospheric stress in this normally quiet part of the system.

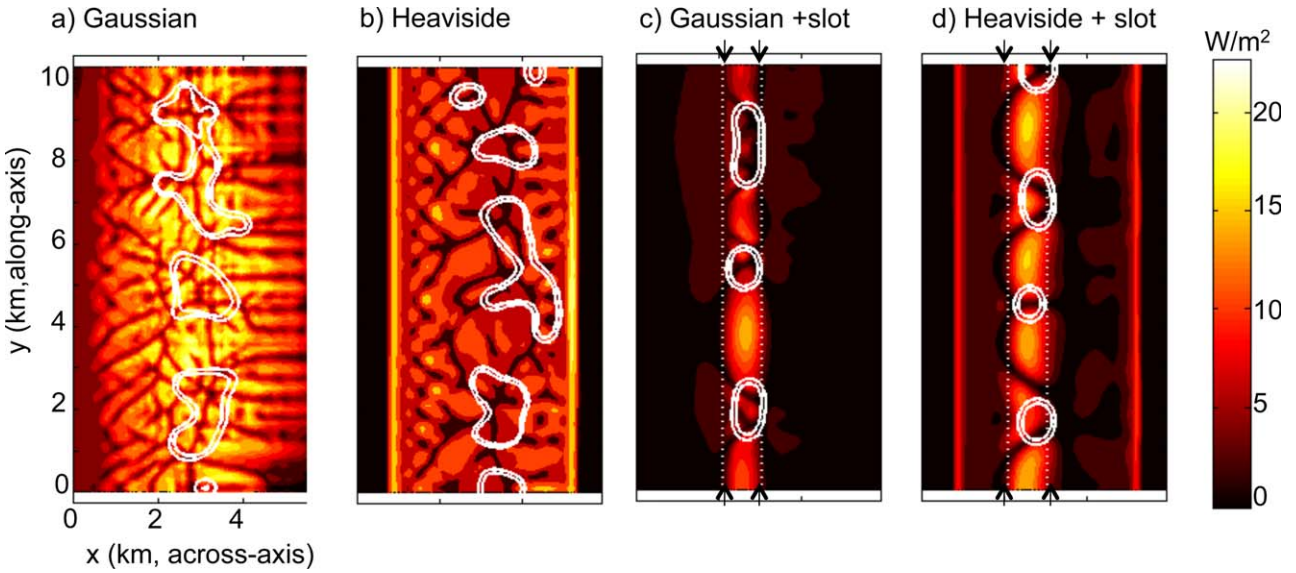

Figure 8. Patterns of heat flux extraction at the base of the hydrothermal layer. Thick white lines mark the 200 and 300°C isotherms. (a) Model with a "Gaussian-like" across-axis basal temperature gradient (65°C/km across axis) and uniform permeability. (b) Model with a "Heaviside-like" across-axis basal temperature gradient and uniform permeability (see Figure 3). (c) Model with a "Gaussian-like" across-axis basal temperature gradients and a higher-permeability slot. (d) Model with a "Heaviside-like" across-axis basal temperature gradient and a higher-permeability slot.

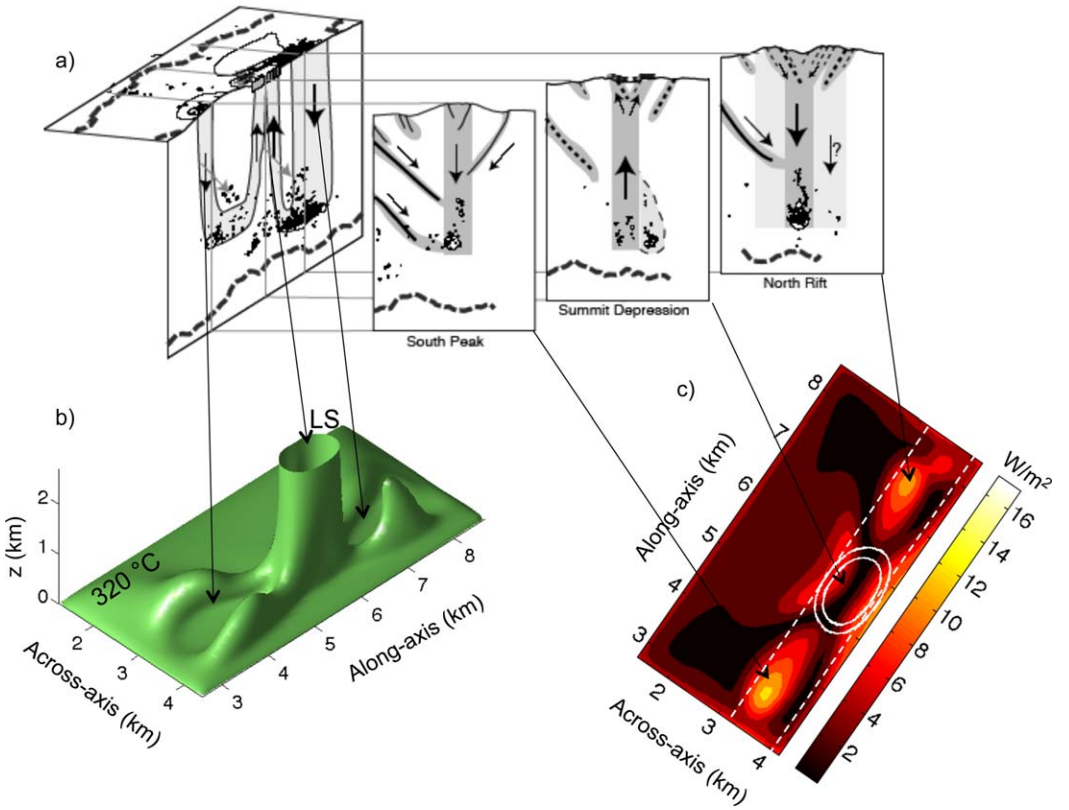

Figure 9. Conceptual model for subseafloor flow geometry beneath the Lucky Strike hydrothermal vent field. In this model, a 3 km wide by 6 km long high-temperature (Heaviside-profile with maximum at 500°C) zone is included at the base of the model to mimic the AMC. Because the axial graben is near the Eastern border of the AMC (Figure 1), we emplaced the high-permeability slot (1 km wide, 10 km long, and 3 km deep) on the eastern side of the model's high-temperature basal anomaly. LS: Lucky Strike vent fields. (a) The 2008–2009 earthquake hypocenters and suggested hydrothermal flow pathways [from *Crawford et al*., 2013]. Clusters of microseismic activity 1 km to the North and South of the venting site suggest along-axis fluid flow. (b) The 3-D 320°C isotherm in the computing box. (c) Heat extraction at the base of the box, colors and contours as in Figure 8.

While higher permeabilities may be inferred in the narrow graben that dissects the Lucky Strike volcano (Figure 1), faulting in this graben probably does not extend all the way down to the AMC [*Barreyre et al*., 2012; *Singh et al*., 2006]. Our models suggest, however, that high permeabilities are required from the seafloor down to near the top of the AMC in order to focus basal heat extraction along axis. We propose that dikes propagating from the AMC toward the seafloor within the graben zone may damage the lithosphere below the level of intense faulting and fissuring associated with the axial graben, creating a high-permeability crack network. Dikes may actually contribute to the formation of the axial graben if a significant proportion do not reach the seafloor, as is commonly observed in Iceland and Afar [*Rubin and Pollard*, 1988; *Rubin*, 1992] and has been proposed for the EPR [*Hooft et al*., 1996; *Soule et al*., 2009].

The number of hydrothermal cells along-axis depends on the along-axis extent of the basal heat source. In regions of the axis that are not underlain by an AMC, the temperatures at the base of the permeable hydrothermal layer are probably too low for high-temperature hydrothermal/convective modes to arise. If we limit the basal heating to a Heaviside-like region 6–7 km long, consistent with the along-axis extent of the Lucky Strike AMC, only one vent field would form (Figure 9). The modeled heat flux of this vent field, assuming a slot permeability of 3×10^{-14} m^2, is about 130 MW, which is at the lower end of heat flux estimates for Lucky Strike [*Barreyre et al*., 2012]. Increasing the permeability in the slot increases the vent heat flux, but gives rise to a second vent pipe a few kilometers further along-axis. Although the Evan hydrothermal area (Figure 1) is located at about the same distance from the main field as in this model, its output appears to be much lower than the model would predict. When visited in 2006, this vent area covered only a few hundred square meters and displayed only diffuse vents [*Ballu and The Graviluck Scientific Party*, 2006]. It is not known whether the fluids vented at Evan have deep origins (i.e., near the magma chamber).

Two additional factors that our models do not account for could allow a stronger flow at Lucky Strike without requiring another upwelling zone. One is the along-axis variation in the depth to the AMC and the other is the seafloor relief. The Lucky Strike main field is located above a local high of the AMC roof [*Singh et al*., 2006] and the two seismic clusters interpreted as the base of recharge paths occur in the vicinity of local lows of the AMC roof [*Crawford et al*., 2013]. These local lows correspond to 10°–20° slopes of the AMC roof [*Crawford et al*., 2013], sufficiently steep to focus upflow zones upslope, favoring the formation of convective systems with a single discharge zone [*Fontaine et al*., 2008]. In other words, the highest effective permeability allowed while generating a single vent field would increase in models with a sloping base. This could allow a single vent field with heat flux closer to Lucky Strike estimates (>200 MW) [*Barreyre et al*., 2012]. As shown in *Fontaine et al*. [2011], this roof topology could result from or be augmented by the heat extraction variations along the convective cell, with higher extraction below the recharge regions than below discharge regions.

Our models also do not account for seafloor relief, which has been shown to influence subseafloor hydrothermal cell geometry [*Bani-Hassan et al*., 2012], with bathymetric highs focusing and stabilizing upflows. *Bani-Hassan et al*. [2012] specifically investigate the case of the Lucky Strike hydrothermal vent system and conclude that the topography of the volcanic edifice stabilizes the location of the main vent field at its top. However, they only considered two-dimensional across-axis models of hydrothermal convection. Whether along-axis seafloor relief affects hydrothermal cell geometry at Lucky Strike is debatable. The main Lucky Strike field is immediately surrounded by three bathymetric highs, and the southern microseismic cluster interpreted as the trace of a recharge path is located below the one of these bathymetric high (a volcanic mound; Figure 1). Synthetic models from *Bani-Hassan et al*. [2012] would predict the contrary, i.e., upflow zones below bathymetric highs and downflow zones beneath bathymetric lows. The along-axis variations in the depth to the AMC (discussed above) may interfere with seafloor relief effects, and the combined result determines the position and geometry of the hydrothermal cells at Lucky Strike.

Our modeling formalism is based on a constant temperature bottom boundary condition inferred from the presence of the Lucky Strike AMC. The roof of this AMC is assumed to represent an isothermal surface (1000°C) that is taken into account by introducing a 3×6 km^2 high-temperature surface at the base of the model box (Figure 9). *Cann and Strens* [1982] and more recently *Lowell et al*. [2013] suggest that the driving force behind hydrothermal activity in magma-rich systems is not the temperature but rather the local release of latent heat of crystallization within the molten AMC. Whether a heat flux or bottom temperature boundary condition should be used to model hydrothermal activity is difficult to assess. The formalisms meet if the heat flux condition is applied at the base of the system such that magmatic temperatures (>1000°C) are reached there, but hydrothermal heat loss is limited to regions whose temperatures are below a threshold value (500–800°C). In this alternative approach, we would introduce a heat flux boundary condition at the base of the model box, with a 3×6 km^2 high heat flux surface mimicking the AMC and the afferent release of latent heat. Although we did not run such a numerical simulation, the introduction of this high heat flux surface would probably result in similar features to our temperature-based bottom boundary condition. If high heat flux was imposed over the entire bottom surface, multiple km-wide hydrothermal pipes with disordered distribution would probably form, as thermal instabilities are free to arise anywhere above a large high heat flux surface (18–20 km^2 in our model), as was the case in Figure 2. An along-axis oriented system of discharge and recharge would therefore require the introduction of a higher-permeability slot in the model, consistent with our main conclusion. Local heterogeneities in latent heat release within the AMC could induce local variations of basal heat flux that would focus flow in the hydrothermal layer, but it is difficult to quantify these processes, which are controlled by magma chamber dynamics (convection, replenishment. . .) for which we have few constraints. The AMC roof topology at Lucky Strike could reflect such heterogeneities, with the expected hydrothermal flow focusing effects induced by the basal slopes that we discussed above.

Our modeling approach uses a single-phase formalism that models the flow of seawater in the single-phase regime, but only the flow of vapor-like fluids in the two-phase regime. Lucky Strike high-temperature chimneys vent fluids that are both "vapor-like" (i.e., salinity < seawater) and "brine-like" fluids (salinity > seawater): emanations slightly saltier than seawater were first recorded in 2008 [*Pester et al*., 2011], whereas the vents were vapor-like before. Samples collected on a yearly basis between 2009 and 2013 confirm the venting of brine-like fluids at a few high-temperature sites [V. Chavagnac, personal communication, 2014].

This indicates that active phase separation processes and resulting two-phase flow are taking place in the Lucky Strike crust, which our model does not fully account for. Very few studies have investigated two-phase flow in MOR hydrothermal systems and all are limited to 2-D geometries. *Han et al*. [2013], *Singh et al*. [2013], and *Coumou et al*. [2009b] are state of the art studies of these processes, but their model set-ups are limited to 1–1.5 km deep systems. However, simulations run by *Coumou et al*. [2009b] include pressures that cover the range within the Lucky Strike system, because they ran simulations for seafloor depths of 1.5, 2.5, and 3.5 km corresponding to model pressure ranges of 150–250, 250–350, and 350–450 bars, respectively. Their minimum top pressure value of 150 bars is commensurate with the minimum top pressure value of 170 bars at Lucky Strike, and their maximum bottom pressure (450 bars) is close to the ~470 bars pressure at the bottom of the Lucky Strike system. Their simulations in the deepest model—using a 3.5 km long and 1 km deep box, 450 bars bottom pressure, a permeability of 10^{-14} m^2, and a heat flux of 60 W/m^2 (consistent with a few hundred of MW if the system were a few km wide across axis)—show the formation of several two-phase (vapor-liquid) rising plumes that merge to form a single upflow pipe. Brines formed by condensation sink and are stored in the bottom boundary layer where they remain immobile and stably stratified while buoyant vapors escape the boundary layer. This situation prevails as long as brines do not completely fill the boundary layer. This situation is similar to the single-phase system we model at Lucky Strike: with only the vapor phase flowing in the two-phase boundary layer. Brine-like fluids that discharge at some vents could result from boiling of the rising fluid and the production of a two-phase vapor-liquid zone at shallower depths. At the pressures consistent with these shallower depths (i.e., 150 bars at the top), *Coumou et al*.'s [2009b] experiment reveals the formation of a liquid-vapor upflow zone that favors episodic venting of brine-like fluids over a few years' period. Alternatively, brine-like venting at Lucky Strike could result from the depletion of the dense brine stored in the bottom boundary that has returned to the single-phase area [*Schoofs and Hansen*, 2000], prefiguring a more secular cooling process. Constraining the dynamics of two-phase flow at Lucky Strike would require a longer time series analysis of the salinity of vents and a dedicated two-phase flow modeling study using the Lucky Strike site geometry.

Highly fissured and therefore more permeable narrow axial zones are extensively documented along faster spreading ridges [e.g., *Normark*, 1986; *Haymon et al*., 1991; *Embley et al*., 2000; *Ferrini et al*., 2007; *Hearn et al*., 2013]. Km-wide hydrothermal convection cells inferred from seismicity along the EPR at 9°50′N [*Tolstoy et al*., 2008] are also difficult to reconcile with "nested-pipe" cell geometries [*Coumou et al*., 2009a]. We propose that across-axis permeability variations may also play a first-order role on the production and geometry of these km-wide convection cells. Verifying this and constraining its effects and implications would require models that incorporate the specificities of this fast spreading ridge section (e.g., a shallower and more continuous axial magma chamber, lesser axial relief and along-axis permeability variations due to ridge discontinuities).

6. Conclusions

We ran a series of three-dimensional numerical models to study the flow architectures of high-temperature subseafloor hydrothermal systems. The primary goals of our work are to constrain the physical parameters controlling the formation of hydrothermal flow with elongated convection cells and to highlight the relationships between this flow geometry and microearthquake distribution patterns. Our study is principally based on observations from the Lucky Strike vent field, where a unique seafloor observatory of hydrothermal, tectonic, and volcanic processes has been operating since 2006.

An along-axis flow geometry is favored by a km-wide along-axis high-permeability "slot." The circulation is composed of km-wide pipe-like upflow zones with recharge zones in between. Across-axis temperature or heat flux gradients at the base of the hydrothermal layer may also contribute to this flow organization, due to the across-axis bounds of the axial magma chamber and/or to localized release of latent heat of crystallization. The more the basal temperature/heat flux is focused near the rise axis, the lower the permeability contrast that is needed between the slot and the surrounding rocks in order to generate along-axis flow. At Lucky Strike, the high-permeability slot is located beneath and at least partly due to a central axial graben that dissects the volcanic edifice. The formation of a single major vent field, as is the case at Lucky Strike, may also require some dynamical forcing due to magma chamber or seafloor topography.

Our models show that recharge zones correspond to heat extraction highs at the base of the hydrothermal layer, while discharge zones correspond to lows. In our models incorporating a high-permeability slot, highs and lows are kilometer-wide and alternate along-axis below recharge and discharge zones, respectively. Heat extraction highs below recharge zones appear to be the preferential locus of microearthquake activity driven by cracking front propagation and/or magma chamber crystallization and collapse. This alternating pattern of heat extraction highs and lows is in good agreement with the microearthquake data of *Crawford et al*. [2013], which shows the presence of two distinct clusters of microearthquakes above the Lucky Strike magma chamber, 1 km to the north and to the south of the venting site. A high-permeability slot associated with fissured and fractured axial regions of fast/intermediate spreading ridges would likely favor similar along-axis flow geometry, which could explain observations of narrow microseismic cluster zones beneath the EPR at 9°50′N.

Our models do not take into account phase separation, which could also influence flow geometry and locations of heat extractions highs and lows. These processes should be included in future modeling work to assess their role on the chemical and thermal evolutions of vent fluids and distribution of microseismic activity.

Acknowledgments
We thank Robert Lowell, Rob Sohn, and the editor Thorsten Becker for their thorough reviews of earlier versions of this manuscript. This is Institut de Physique du Globe de Paris contribution n° 3549.

References

Antoine, R., D. Baratoux, M. Rabinowicz, F. J. Fontaine, P. Bachèlery, T. Staudacher, G. Saracco, and A. Finizola (2009), Thermal infrared images analysis of a quiescent cone on Piton de la Fournaise volcano: Evidence of convective air flow within an unconsolidated soil, *J. Volcanol. Geotherm. Res.*, *183*, 228–244.

Ballu, V., O. deViron, W. C. Crawford, M. Cannat, and J. Escartin (2012), Long-term observations of seafloor pressure variations at Lucky Strike volcano, Mid-Atlantic Ridge, Abstract OS13B-1730 presented at 2012 Fall Meeting, AGU, San Francisco, Calif.

Bani-Hassan, N., K. Iyer, L. H. Rüpke, and A. Borgia (2012), Controls of bathymetric relief on hydrothermal fluid flow at mid-ocean ridges, *Geochem. Geophys. Geosyst.*, *13*, Q05002, doi:10.1029/2012GC004041.

Barreyre, T., J. Escartín, R. Garcia, M. Cannat, E. Mittelstaedt, and R. Prados (2012), Structure, temporal evolution, and heat flux estimâtes from the Lucky Strike deep-sea hydrothermal field derived from seafloor image mosaics, *Geochem. Geophys. Geosyst.*, *13*, Q04007, doi:10.1029/2011GC003990.

Cann, J. R., and M. R. Strens (1982), Black smoker fueled by freezing magma, *Nature*, *298*, 147–149, doi:10.1038/298147a0.

Cannat, M., J. Cann, and J. Mclennan (2004), Some hard rock constraints on the supply of heat to Mid-Ocean Ridges, in *Hydrothermal Interactions Between the Lithosphere and Oceans, Geophys. Monogr. Ser.*, vol. 148, edited by C. R. German et al., pp. 111–149, AGU, Washington, D. C.

Cannat, M., P.-M. Sarradin, J. Blandin, J. Escartin, A. Colaco, and the MoMAR-Demo Scientific Party (2011), MoMar-Demo at Lucky Strike. A near-real time multidisciplinary observatory of hydrothermal processes and ecosystems at the Mid-Atlantic Ridge, Abstract OS22A-05 presented at 2011 Fall Meeting, AGU, San Francisco, Calif., 5–9 Dec.

Charlou, J. L., J. P. Donval, E. Douville, P. Jean-Baptiste, J. Radford-Knoery, Y. Fouquet, A. Dapoigny, and M. Stievenard (2000), Compared geochemical signatures and the evolution of Menez Gwen (37°50′N) and Lucky Strike (37°17′N) hydrothermal fluids, south of the Azores Triple Junction on the Mid-Atlantic Ridge, *Chem. Geol.*, *171*, 49–75.

Coumou, D., T. Driesner, S. Geiger, A. Paluszny, and C. A. Heinrich (2009a), High-resolution three-dimensional simulations of mid-ocean ridge hydrothermal systems, *J. Geophys. Res.*, *114*, B07104, doi:10.1029/2008JB006121.

Coumou, D., T. Driesner, P. Weis, and C. A. Heinrich (2009b), Phase separation, brine formation, and salinity variation at Black Smoker hydrothermal systems, *J. Geophys. Res.*, *114*, B03212, doi:10.1029/2008JB005764.

Crawford, W. C., S. C. Singh, T. Seher, V. Combier, D. Dusunur, and M. Cannat (2010), Crustal structure, magma chamber and faulting beneath the Lucky Strike hydrothermal vent field, in *Diversity of Hydrothermal Systems on Slow Spreading Ocean Ridges, Geophys. Monogr. Ser.*, vol. 188, edited by P. A. Rona et al., pp. 113–132, AGU, Washington, D. C.

Crawford, W. C., A. Rai, S. C. Singh, M. Cannat, J. Escartin, H. Wang, R. Daniel, and V. Combier (2013), Hydrothermal seismicity beneath the summit of Lucky Strike volcano, Mid-Atlantic Ridge, *Earth Planet. Sci. Lett.*, *373*, 118–128, doi:10.1016/j.epsl.2013.04.028.

Embley, R. W., W. W. Chadwick, M. R. Perfit, M. C. Smith, and J. R. Delaney (2000), Recent eruptions on the CoAxial segment of the Juan de Fuca Ridge: Implications for mid-ocean ridge accretion processes, *J. Geophys. Res*, *105*, 16,501–16,525, doi:10.1029/2000JB900030.

Escartin, J., A. Soule, A. Bezos, M. Cannat, D. J. Fornari, V. Ballu, and S. Humphris (2006), Patterns of volcanism and tectonism at a slow-spreading segment of the Mid-Atlantic Ridge (Lucky Strike, 37°N): Preliminary results from near-bottom geological and geophysical surveys, *Eos Trans. AGU*, *87*(52), Fall Meet. Suppl., Abstract B33D-05.

Ferrini, V., D. J. Fornari, and T. M. Shank (2007), Submeter bathymetric mapping of volcanic and hydrothermal features on the East Pacific Rise crest at 9°50′N, *Geochem. Geophys. Geosyst.*, *8*, Q01006, doi:10.1029/2006GC001333.

Fontaine, F. J., and W. S. D. Wilcock (2007), Two-dimensional numerical models of open-top hydrothermal convection at high Rayleigh and Nusselt numbers: Implications for mid-ocean ridge hydrothermal circulation, *Geochem. Geophys. Geosyst.*, *8*, Q07010, doi:10.1029/2007GC001601.

Fontaine, F. J., M. Cannat, and J. Escartin (2008), Hydrothermal circulation at slow-spreading mid-ocean ridges: The role of along-axis variations in axial lithospheric thickness, *Geology*, *36*, 759–762, doi:10.1130/G24885A.1.

Fontaine, F. J., J.-A. Olive, M. Cannat, J. Escartin, and T. Perol (2011), Hydrothermally-induced melt lens cooling and segmentation along the axis of fast-and inter- mediate-spreading centers, *Geophys. Res. Lett.*, *38*, L14307, doi:10.1029/2011GL047798.

Fouquet, Y., H. Ondreas, J. L. Charlou, J. P. Donval, J. Radford-Knoery, I. Costa, N. Lourenco, and M. K. Tivey (1995), Atlantic lava lakes and hot vents, *Nature*, *377*, 201–201.

Geiger, S., T. Driesner, C. A. Heinrich, and S. K. Matthäi (2005), On the dynamics of NaCl-H_2O fluid convection in the Earth's crust, *J. Geophys. Res.*, *110*, B07101, doi:10.1029/2004JB003362.

Han, L., R. P. Lowell and K. C. Lewis (2013), The dynamics of two-phase hydrothermal systems at a seafloor pressure of 25 MPa, *J. Geophys. Res. Solid Earth*, *118*, 2635–2647, doi:10.1002/jgrb.50158.

Haymon, R. M., D. J. Fornari, and M. Edwards (1991), Hydrothermal vent distribution along the East Pacific Rise crest (9°09′–54′N) and its relationship to magmatic and tectonic processes on fast-spreading mid-ocean ridges, *Earth Planet. Sci. Lett.*, *104*, 513–534.

Hearn, C. K., K. L. Homola, and H. P. Johnson (2013), Surficial permeability of the axial valley seafloor: Endeavour Segment, Juan de Fuca Ridge, *Geochem. Geophys. Geosyst.*, *14*, 3409–3424.

Hirth, G., J. Escartin, and J. Lin (1998), The rheology of the lower oceanic crust: Implications for lithospheric deformation at mid-ocean ridges, in *Faulting and Magmatism at Mid-Ocean Ridges, Geophys. Monogr. Ser.*, vol. 106, edited by W. R. Buck et al., pp. 291–303, AGU, Washington, D. C.

Hooft, E. E. E., H. Schouten, and R. S. Detrick (1996), Constraining crustal emplacement processes from the variation in Layer 2A thickness at the East Pacific Rise, *Earth Planet. Sci. Lett.*, *142*, 289–309.

Humphris, S. E., D. J. Fornari, D. S. Scheirer, C. R. German, and L. M. Parson (2002), Geotectonic setting of hydrothermal activity on the summit of Lucky Strike Seamount (37°17′N, Mid-Atlantic Ridge), *Geochem. Geophys. Geosyst.*, *3*(8), doi:10.1029/2001GC000284.

Langmuir, C., et al. (1997), Hydrothermal vents near a mantle hotspot; the Lucky Strike vent field at 37°N on the Mid-Atlantic Ridge, *Earth Planet. Sci. Lett.*, *148*, 69–91.

Lowell, R. P., and L. N. Germanovich (2004), Hydrothermal processes at mid-ocean ridges: Results from scale analysis and single-pass models, in *Mid-Ocean Ridges: Hydrothermal Interactions Between the Lithosphere and Oceans, Geophys. Monogr. Ser.*, vol. 148, edited by C. R. German et al., pp. 110–127, AGU, Washington, D. C.

Lowell, R. P., A. Farough, J. Hoover and K. Cummings (2013), Characteristics of magma-driven hydrothermal systems at oceanic spreading centers, *Geochem. Geophys. Geosyst.*, *14*, 1756–1770, doi:10.1002/ggge.20109.

Normark, W. R. (1986), Submarine fissure eruptions and hydrothermal vents on the southern Juan de Fuca Ridge: Preliminary observations from the submersible Alvin, *Geology*, *14*, 823–827.

Ondréas, H., M. Cannat, Y. Fouquet, A. Normand, P. M. Sarradin, and J. Sarrazin (2009), Recent volcanic évents and the distribution of hydrothermal venting at the Lucky Strike hydrothermal field, Mid Atlantic Ridge, *Geochem. Geophys. Geosyst.*, *10*, Q02006, doi:10.1029/2008GC002171.

Pester, N. J., E. P. Reeves, M. E. Rough, K. Ding, J. S. Seewald, and W. E. Seyfried Jr. (2012), Subseafloor phase equilibria in high-temperature hydrothermal fluids of the Lucky Strike Seamount (Mid-Atlantic Ridge, 37°17′N), *Geochim. Cosmochim. Acta, 90*, 303–322, doi:10.1016/j.gca.2012.05.018.

Rabinowicz, M., J. Boulègue, and P. Genthon (1998), Two- and three-dimensional modeling of hydrothermal convection in the sedimented Middle Valley segment, Juan de Fuca Ridge, *J. Geophys. Res.*, *103*, 24,045–24,066.

Rabinowicz, M., J.-C. Sempére, and P. Genthon (1999), Thermal convection in a vertical permeable slot: Implications for hydrothermal circulation along mid-ocean ridges, *J. Geophys. Res.*, *104*, 29,275–29,292.

Rubin, A. M., and D. D. Pollard (1988), Dike-induced faulting in rifts zones of Afar and Iceland, *Geology*, *16*, 413–417.

Rubin, A. M. (1992), Dike-induced faulting and graben subsidence in volcanic rift zones, *J. Geophys. Res.*, *97*, 1839–1858, doi:10.1029/91JB02170.

Scheirer, D. S., D. J. Fornari, S. E. Humphris, and S. Lerner (2000), High-resolution seafloor mappling using the DSL-120 sonar system: Quantitative assessment of sidescan and phase-bathymetry data from the Lucky Strike segment of the Mid-Atlantic Ridge, *Mar. Geophys. Res.*, *21*, 121–142.

Schoofs, S., and U. Hansen (2000), Depletion of a brine layer at the base of the ridge-crest hydrothermal system, *Earth Planet. Sci. Lett.*, *180*, 341–353.

Singh, S., R. P. Lowell, and K. C. Lewis (2013), Numerical modeling of phase separation at Main Endeavour Field, Juan de Fuca Ridge, *Geochem. Geophys. Geosyst.*, *14*, 4021–4034, doi:10.1002/ggge.20249.

Singh, S. C., W. C. Crawford, H. Carton, T. Seher, V. Combier, M. Cannat, J. P. Canales, D. Düsünür, J. Escartin, and J. M. Miranda (2006), Discovery of a magma chamber and faults beneath a Mid-Atlantic Ridge hydrothermal field, *Nature*, *442*, 1029–1032.

Sohn, R. A., S. C. Webb, J. A. Hildebrand and B. D. Cornuelle (1997), Three-dimensional tomographic velocity structure of upper crust, Coaxial segment, Juan de Fuca Ridge: Implications for on-axis evolution and hydrothermal circulation, *J. Geophys. Res.*, *102*, 17,679–17,695, doi:10.1029/97JB00592.

Sohn, R. A., J. A. Hildebrand, and S. C. Webb (1999), A microearthquake Survey of the high-temprature vent fields on the volcanically active East Pacific Rise (9°50′N), *J. Geophys. Res.*, *104*, 25,367–25,378.

Sohn, R. A., A. H. Barclay, and S. C. Webb (2004), Microearthquake patterns following the 1998 eruption of Axial Volcano, Juan de Fuca Ridge: Mechanical relaxation and thermal strain, *J. Geophys. Res.*, *109*, B01101, doi:10.1029/2003JB002499.

Soule, S. A., J. Escartin, and D. J. Fornari (2009), A record of eruption and intrusion at a fast spreading ridge axis: Axial summit trough of the East Pacific Rise at 9–10°N, *Geochem. Geophys. Geosyst.*, *10*, Q10T07, doi:10.1029/2008GC002354.

Tivey, M. A., and H. P. Johnson (2002), Crustal magnetization reveals subsurface structure of Juan de Fuca Ridge hydrothermal vent fields, *Geology*, *30*, 979–982, doi:10.1130/0091–7613.

Tolstoy, M., F. Waldhauser, D. R. Bohnenstiehl, R. T. Weekly, and W. Y. Kim (2008), Seismic identification of along-axis hydrothermal flow on the East Pacific Rise, *Nature*, *451*, 181–184, doi:10.1038/nature06424.

Wilcock, W. S. D. (1998), Cellular convection models of mid-ocean ridge hydrothermal circulation and the temperatures of black smoker fluids, *J. Geophys. Res.*, *103*, 2585–2596.